

Impurity sputtering model for ICRF edge plasma-surface interactions

Quan-Zhi Zhang(张权治), Ze-Xuan Liu(刘泽璇), Fang-Fang Ma(马方方), Lei-Yu Zhang(张雷宇), and Nosir Matyakubov

Citation: Chin. Phys. B, 2025, 34 (**3**): 035201. DOI: 10.1088/1674-1056/ada437
Journal homepage: http://cpb.iphy.ac.cn; http://iopscience.iop.org/cpb

What follows is a list of articles you may be interested in

Three-dimensional simulations of RF wave propagation and power coupling in cold magnetized plasma near an ICRF antenna

Lei-Yu Zhang(张雷宇), Yi-Xuan Li(李屹轩), and Quan-Zhi Zhang(张权治)
Chin. Phys. B, 2025, 34 (**2**): 025204. DOI: 10.1088/1674-1056/ad9a9c

Characteristics of the electromagnetic wave propagation in magnetized plasma sheath and practical method for blackout mitigation

Xiang Wu(吴翔), Jiahui Zhang(张珈珲), Guoxiang Dong(董果香), and Lei Shi(石磊)
Chin. Phys. B, 2024, 33 (**5**): 055201. DOI: 10.1088/1674-1056/ad24d4

Drift surface solver for runaway electron current dominant equilibria during the current quench

Lu Yuan(袁露) and Di Hu(胡地)
Chin. Phys. B, 2023, 32 (**7**): 075208. DOI: 10.1088/1674-1056/acc1d7

Modeling of beam ions loss and slowing down with Coulomb collisions in EAST

Yifeng Zheng(郑艺峰), Jianyuan Xiao(肖建元), Baolong Hao(郝保龙), Liqing Xu(徐立清), Yanpeng Wang(王彦鹏), Jiangshan Zheng(郑江山), and Ge Zhuang(庄革)
Chin. Phys. B, 2022, 31 (**7**): 075201. DOI: 10.1088/1674-1056/ac5883

Estimation of tungsten production from the upper divertor in EAST during edge localized modes

Jing Ou(欧靖), Nong Xiang(项农), Zong-Zheng Men(门宗政), Ling Zhang(张凌), Ji-Chan Xu(许吉禅), Wei Gao(高伟)
Chin. Phys. B, 2019, 28 (**12**): 125201. DOI: 10.1088/1674-1056/ab5279

COMPUTATIONAL PROGRAMS FOR PHYSICS

Impurity sputtering model for ICRF edge plasma–surface interactions

Quan-Zhi Zhang(张权治)[1,†,‡], Ze-Xuan Liu(刘泽璇)[1,†], Fang-Fang Ma(马方方)[1], Lei-Yu Zhang(张雷宇)[1], and Nosir Matyakubov[2,3]

[1] *School of Physics, Dalian University of Technology, Dalian* 116024, *China*
[2] *Department of Physics, Urgench State University, Urgench* 220100, *Uzbekistan*
[3] *School of Engineering, New Uzbekistan University, Tashkent* 100007, *Uzbekistan*

(Received 31 October 2024; revised manuscript received 26 December 2024; accepted manuscript online 31 December 2024)

One of the primary concerns associated with ion cyclotron resonance heating (ICRH) is the enhanced impurity sputtering resulting from radio frequency (RF) sheath formation near plasma-facing components (PFCs), such as limiters. Developing a sputtering model integrated with RF sheath simulations allows for a more comprehensive understanding of the kinetic behavior of incident ions and their interactions with the limiter surface. We accordingly develop an impurity sputtering model "PMSAD", which computes the sputtering yield (amount of impurity) on the limiter surface based on incident ion characteristics and predicts the spatial distribution of impurities. The model provides a robust method for understanding and analyzing the impurity sputtering process from limiter surfaces, which is crucial for preventing ICRH surface erosion and reducing edge and core plasma contamination.

Keywords: ion cyclotron resonance heating (ICRH), radio frequency (RF) sheath, physical sputtering

PACS: 52.25.Xz, 52.40.Fd, 52.65.–y, 28.52.Av

DOI: 10.1088/1674-1056/ada437 **CSTR:** 32038.14.CPB.ada437

1. Introduction

Nuclear fusion is considered a clean and abundant energy source in the future. It releases a tremendous amount of energy in the process of fusing two nuclei into elements with a smaller total mass.[1] Ion cyclotron resonance heating (ICRH) is an auxiliary heating technique used in nuclear fusion device, which efficiently transfers electromagnetic energy to plasma ions through the resonance of radio frequency waves in the plasma, enabling them to reach the high temperatures required for fusion.[2–4] The ICRH system is cost-effective, without a density limit, and suitable for large-scale fusion devices.[5] The International Thermonuclear Experimental Reactor (ITER) plans to use ICRH as one of the heating methods.[6]

The ICRH antenna emits radio frequency (RF) waves at tens of megahertz, transferring electromagnetic energy to the ions via ion cyclotron resonance. A Faraday screen acts as a metallic barrier between the antenna and the plasma, isolating the antenna current from the electric field in the plasma. Additionally, there are metallic devices such as limiters near the Faraday screen. These components in contact with the plasma are referred to as plasma-facing components (PFCs). During ICRH operation, a radio frequency plasma sheath forms on the surfaces of the ICRH antenna, Faraday screen, limiters, and other PFCs.[5,7] These plasma sheaths are primarily driven by RF voltages, hence they are referred to as RF sheaths.[8] Due to the presence of the sheath, a potential drop develops from the plasma region to PFC surfaces, which creates an electric field that accelerates the heavy ions within the sheath up to hundreds of eV, leading to the enhanced bombardment of the PFC and the impurity sputtering phenomenon. Different plasma background densities, magnetic fields, magnetic field directions, and bias voltages can all affect the ion dynamics within the RF sheath, subsequently influencing the impurity sputtering on the material surface.[9] Numerous metallic impurities near the Faraday screen were observed experimentally, which resulted from the impurity sputtering phenomenon.[10] In Alcator C-Mod, Wukitch *et al.* presented circumstantial evidence that suggests RF-enhanced sheaths are the most likely erosion mechanism.[11]

Sputtered impurity particles from the PFCs can contaminate the plasma, which gives rise to some plasma instabilities and reduces the performance of ICRH.[10,12] Therefore, the enhanced impurity sputtering is a critical challenge for ICRH in tokamaks. Tungsten is a primary candidate material for PFCs because of its high melting point, excellent sputtering resistance, and low hydrogen retention, and is being widely applied in nuclear fusion devices.[13] However, tungsten has a high atomic number of 74, enabling it to radiate significant

[†] Authors contributed equally to this work.
[‡] Corresponding author. E-mail: qzzhang@dlut.edu.cn
© 2025 Chinese Physical Society and IOP Publishing Ltd. All rights, including for text and data mining, AI training, and similar technologies, are reserved.

energy during a discharge. The energy loss through impurity radiation may cool the plasma down, ultimately halting the fusion reactions.[14] Therefore, several experimental studies have been conducted on tungsten impurity sputtering induced by ICRH. Urbanczyk *et al.* proposed that the tungsten components magnetically connected to the ICRH antenna exhibit substantial impurity sputtering, which may contribute more to the core tungsten content than the sources from the divertor.[15] Other studies also indicate that the application of ICRH significantly elevates tungsten impurity levels. For example, replacing a 3.5 MW neutral beam injection (NBI) with 300 kW of ICRH power results in a sixfold increase in tungsten content, while further increasing the ICRH power to 750 kW leads to a tenfold increase.[16]

Elias further presented a 1D fluid plasma sheath model with a magnetic field at a specific angle, which effectively captures the sputtering yield from the Faraday screen through the momentum transport of ions.[17] He also presented a hybrid particle-in-cell (hPIC) model to capture the kinetic behavior of the ions and analyze the kinetic ion energy-angle distributions (IEADs) impacting the RF antenna.[18] A modified test involving two-strap ion cyclotron range of frequency (ICRF) antennas in ASDEX Upgrade, featuring narrow straps, demonstrated a reduction of up to 40% in the tungsten concentration.[19] Li *et al.* also studied the sputtering of tungsten on the divertors in the scrape-off layer (SOL) of the WEST tokamak.[20] According to our knowledge, current research primarily focuses on the sputtering processes on Faraday screens, antennas, and divertors, with little investigation into the sputtering of ICRF limiters. These limiters are magnetically connected to the ICRF antenna and play a significant role in the distribution of tungsten impurity content during ICRH. Minimizing impurity sputtering of ICRF-limiters is essential to avoid erosion and contamination of ICRH systems. Moreover, the experimental diagnostic methods for studying impurities in ICRF heating are somewhat limited. For instance, the visible spectroscopy data from the WEST experiment were not fully calibrated, which restricted the analyses to qualitative studies only.[16,21,22] A self-consistent model that can simultaneously simulate both ion dynamics in the vicinity of antennas and the sputtering process on the limiter surface is urgently required.

Due to the sensitivity of sputtering process to impact ions densities, velocities and angles, the kinetic descriptions of the ion energy-angle distribution information at the surface are required when modeling the impurity sputtering of PFC.[17,23] Therefore, in this work, we present a simulation technique composed of the RF sheath and sputtering models. The RF sheath simulation is based on a two-dimensional particle-in-cell (PIC) model to simulate the plasma kinetic behavior at the boundary of the antenna and limiter.[24,25] The sputtering model takes into account the energy and angle dependence of the incident ions, simulating the impurity sputtering process. The tungsten impurity sputtering yield at various locations on the limiter can be quantitatively calculated, which may subsequently be used to examine the influence of impurities on heating within the core plasma region of a fusion reactor.

This paper focuses on a modeling technique that simultaneously calculates the sputtering yield and predicts the spatial distribution of sputtered atoms, an area that has been inadequately addressed in previous research. Section 2 provides a detailed description of the PIC based RF sheath model and the impurity sputtering one. Section 3 presents the simulation results, which include the sputtering yield of the tungsten limiter, the density distribution of the sputtered atoms, and the critical factors influencing the sputtering process.

2. Implementation of the simulation method

Figure 1 displays the flowchart of the impurity sputtering simulation for ICRF plasma–surface interactions, composed of the RF sheath and sputtering models. In the RF sheath model, the magnetic field, RF source, and plasma source are established to simulate the kinetic behavior of plasma boundary between the antenna and limiter. The velocities and positions of ions impacting the limiter surface are subsequently recorded and utilized as input parameters for the sputtering model. By specifying tungsten as the surface material in the sputtering model, we calculate the impurity sputtering yield at various locations and assess the spatial distribution of sputtered atoms.

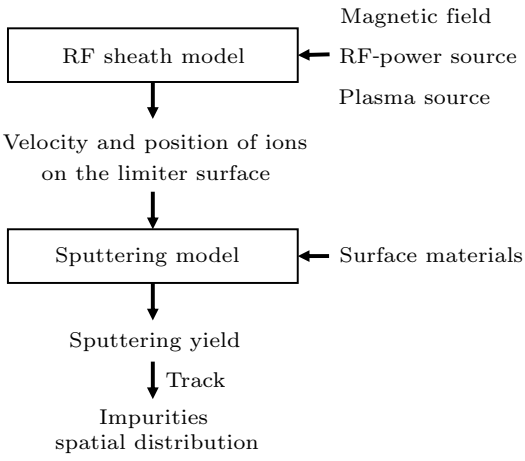


Fig. 1. Flowchart of impurity sputtering simulation for ICRF plasma–surface interactions.

2.1. RF sheath model

The RF sheath model used for this work is a 2D3V PIC model with both kinetic ions and electrons in Cartesian coordinates.[26–28] The PIC method is a very powerful numerical tool that is widely used in plasma simulations, allowing for a self-consistent description of particles and fields. A di-

agram of the general flow of the PIC algorithm is shown in Fig. 2.[29]

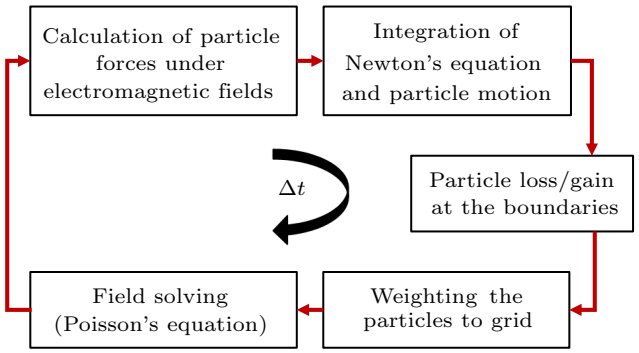


Fig. 2. Logic flow diagram of the PIC algorithm.

The PIC model treats the particles (e.g., ions and electrons) in the plasma as macroparticles (having the same charge-to-mass ratio). Starting from the initial conditions, particles and field values are advanced sequentially in time. The cloud-in-cell (CIC) method[30] is used to weight the macroparticles onto grid points in order to compute the spatial charge density. The spatial potential distribution is obtained by solving the Poisson equation based on the charge density,

$$\nabla^2 \Phi = -\frac{\rho}{\varepsilon_0}. \tag{1}$$

For a two-dimensional model in Cartesian coordinates, the Poisson equation can be discretized as

$$\frac{\Phi_{i-1,j} - 2\Phi_{i,j} + \Phi_{i+1,j}}{\Delta x^2} + \frac{\Phi_{i,j-1} - 2\Phi_{i,j} + \Phi_{i,j+1}}{\Delta y^2} = -\frac{\rho_{i,j}}{\varepsilon_0}. \tag{2}$$

Then it is solved by using the successive over-relaxation (SOR) method to accelerate the convergence as

$$\Phi_{i,j}^{(k+1)} = \omega \Phi_{i,j}^{(k+1)} + (1-\omega)\, \Phi_{i,j}^{(k)}, \tag{3}$$

where the results at steps k and $k+1$ are weighted and averaged to provide the new iteration potential result. ω is the relaxation factor, typically chosen within the range of 0 to 2.[31,32] Here, ρ represents the net charge density, ε_0 is the vacuum permittivity, and Φ denotes the spatial potential. The subscripts i and j correspond to the grid indices in the x and y directions, while the superscript k indicates the iterative time steps. Δx and Δy are the sizes of grids in two directions.

After obtaining the spatial potential, the spatial electric field E_x and E_y can be calculated. Since the electric field, potential, and charge density are all defined at the grid points, a central difference scheme can be employed to compute the electric field in 2D space as follows:

$$\begin{cases} E_x = \dfrac{\Phi_{i-1,j} - \Phi_{i+1,j}}{2\Delta x}, \\ E_y = \dfrac{\Phi_{i,j-1} - \Phi_{i,j+1}}{2\Delta y}. \end{cases} \tag{4}$$

The motion of charged particles is tracked by solving Newton's equations of motion in the given spatial electromagnetic fields. To accurately account for the Lorentz force under the influence of a magnetic field, the Boris method[30] is employed in the simulation to advance the motion of charged particles. The PIC loops are iteratively repeated to self-consistently describe the plasma behavior, including the solution of the sheath on the RF antenna limiter surface.

The geometry region near the ICRF antenna is shown in Fig. 3(a).[33] The background area represents the plasma bulk region. The gray structure connected to the antenna is the limiter, where RF sheaths form on its surface, as shown in the orange areas. The RF sheath accelerates heavy ions from the plasma bulk region to energies of several hundred eV towards the limiter, resulting in the phenomenon of impurity sputtering. Consequently, simulating the RF sheath region at the limiter and plasma boundary, as indicated by the red rectangle in Fig. 3(a), will provide sufficient accuracy.

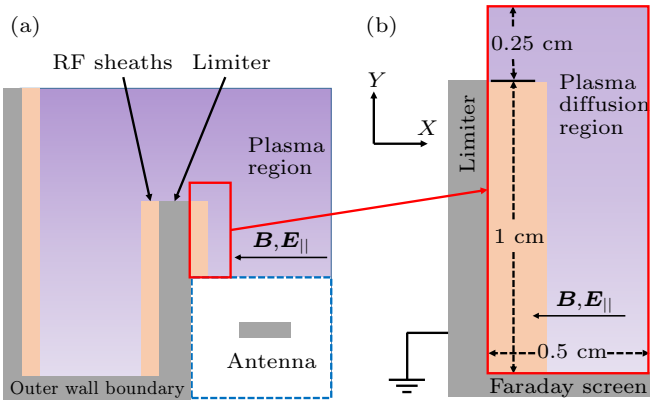


Fig. 3. (a) Schematic of the geometry near the ICRF antenna and (b) schematic of the RF sheath model simulation area.

Figure 3(b) provides a more specific and detailed view of the red rectangle in Fig. 3(a), with annotations indicating the relevant settings for the simulation region. The simulation is organized within a two-dimensional space with the x and y axes designated such that the limiter is positioned along the y-axis, measuring 1 cm in length, and the Faraday screen along the x axis. Additionally, an extending plasma region of 0.25 cm is simulated in the y direction above the limiter, while the simulation region in the x direction is 0.5 cm. Both the limiter and Faraday screen are grounded, the sheath will self-consistently evolve on the limiter surface after a period of calculation. The simulation length chosen in x-axis is large enough to include the whole sheath. As the ICRF antenna produces $E_{\parallel}$ component along magnetic field lines,[34,35] which develops an RF voltage drop near the limiters at the same frequency f of the ICRF, an RF voltage source is assumed to exist at the right boundary of the simulation area. The RF voltage amplitude varies with ICRF-antenna phasing and other conditions, and it typically ranges from several hundred Volts to one

kilo-Volts.[36] Additionally, a DC self-bias voltage V_{DC} develops at the right boundary of the simulation region,[37,38] which is based on the balance of the ion and electron fluxes incident on the limiter. Specifically, at $x = 0.5$ cm, the maximum voltage amplitude V_{RF} remains consistent between $y = 1.25$ cm and $y = 1$ cm; whereas between $y = 1$ cm and $y = 0$ cm, the amplitude of the RF source decreases exponentially to zero (i.e., the voltage transition from $V_{RF}\cos(2\pi ft) + V_{DC}$ to 0). The remaining boundaries are set with Dirichlet boundary conditions (i.e., $\nabla\Phi = 0$). The magnetic field $\boldsymbol{B}$ of 2 T is parallel to the electric field.

A volumetric plasma source is set at the right boundary ($x = 0.5$ cm) of the simulation region shown in Fig. 3(b). Under the influence of electric and magnetic fields, electrons and ions move and gradually evolve into the sheaths on the limiter and Faraday screen. The plasma source density is set according to the density distribution of the scrape-off layer (SOL) plasma along the y-axis derived from Ref. [39]. Specifically, between $y = 1.25$ cm and $y = 1$ cm, the plasma source has a fixed density of 1×10^{18} m^{-3}. From $y = 1$ cm down to $y = 0$ cm, the plasma source density decreases exponentially from 1×10^{18} m^{-3} to 1×10^{16} m^{-3}. At the surfaces of the limiter and Faraday screen, particle boundary conditions are set to absorption. On the limiter surface, the 3D velocity and position of ions are recorded, serving as input parameters for the sputtering model. Charged particles adsorbed on solid surfaces can recombine, forming weakly bound neutral particles that desorb back into the plasma — a process known as particle recycling.[40] The other boundaries are set as particle reflection boundary conditions.

The discharge is studied by applying a voltage waveform of $V_{RF}\cos(2\pi ft)$. The parameters chosen are $f = 37$ MHz and $V_{RF} = 200$ V, 600 V, and 1000 V, which are referenced in Ref. [36]. The grid sizes Δx and Δy are set at 8.33×10^{-5} m uniformly, with the numbers of cells being 60 in x-direction and 150 in y-direction. The time step Δt is taken to be 2×10^{-11} s. The grid size and time step are chosen to resolve the fastest temporal and finest spatial behavior of the particles, specifically $\Delta x \leq \lambda_{De}$ and the Courant limit, $v_t \cdot \Delta t < \Delta x$, where λ_{De} is the Debye length and v_t is the electron thermal velocity.[41] All the presented plasma parameters in this work are calculated after the simulations reach equilibrium by repeating around 500 RF cycles.

2.2. Sputtering model

The basic mechanism of physical sputtering is the transfer of kinetic energy from bombarding ions to target atoms in the solid. If the energy transferred to the target atom is larger than the surface binding energy, then the atom can be ejected from the solid material.[42–44] The developed physical sputtering model is coupled with the sheath model, using the ion energy and angle at the limiter surface as input. The model primarily includes two critical components: the calculation of sputtering yield and the emission of sputtered atoms.

2.2.1. Sputtering yield

The sputtering yield EY is defined as the number of atoms sputtered per incident ion. Numerous factors determine the sputtering yield, with the primary influences being the ions incident energy E_0 and the incident angle α.[45–47] Considering both the energy dependency and the angle one, the sputtering yield $EY(E_0,\alpha)$ derived from Ref. [48] can be written as

$$EY(E_0,\alpha) = EY(E_0,0)\left\{\cos\left[\left(\frac{\alpha}{\alpha_0}\frac{\pi}{2}\right)^c\right]\right\}^{-f} \times \exp\left\{b\left(1-\frac{1}{\cos\left[\left(\frac{\alpha}{\alpha_0}\frac{\pi}{2}\right)^c\right]}\right)\right\}. \quad (5)$$

In this equation, $EY(E_0,0)$ represents the sputtering yield when ions are incident perpendicularly to the surface, capturing the energy dependence of the yield. The subsequent term serves as an angular correction factor accounting for the angular dependence. $EY(E_0,0)$ adopts a relatively new fitting formula proposed in previous research[45] as follows:

$$EY(E_0) = 0.5Q\frac{\left(\frac{E_0}{E_{th}}-1\right)^{\mu}\ln(1+1.2288\varepsilon)}{\lambda+\left(\frac{E_0}{E_{th}}-1\right)^{\mu}\left[\varepsilon+0.1728\sqrt{\varepsilon}+0.008\varepsilon^{0.1504}\right]} \quad (6)$$

with

$$\varepsilon = \frac{a_L}{Z_1Z_2e^2}\frac{M_2}{M_1+M_2}E_0, \quad (7)$$

$$a_L = \left(\frac{9\pi^2}{128}\right)^{1/3}a_B\left(Z_1^{2/3}+Z_2^{2/3}\right)^{-1/2}. \quad (8)$$

Here E_0 is the energy of the incident ions, Z_1 and M_1 are the atomic number and mass of the incident particles, respectively, while Z_2 and M_2 are the atomic number and mass of the target particles, respectively. Here, a_L is called the Lindhard screening length, and a_B is the Bohr radius. E_{th} is the sputtering threshold of the target. In addition, the parameters Q, λ, μ, b, c, f in the formulae are dimensionless empirical constants dependent on the specific sputter–target material combination, which can be obtained by fitting with experimental data.[48] The sputtering yield energy dependence of H^+ ions impacting tungsten target at normal incident angle used in our model is presented in Fig. 4(a). It is evident that as the energy of the incident ions exceeds the sputtering threshold, the sputtering yield initially rises before subsequently declining. This phenomenon occurs because sputtering initiates once the incident ions reach the threshold energy level, leading to a rapid increase in the number of sputtered particles as the ions transfer

additional energy to the wall material. However, as the ion energy continues to rise, the ions begin to penetrate deeper into the material, resulting in a decrease in the number of surface atoms due to the collision cascade effect.[49] This leads to a reduction in the sputtering yield at very high energies.

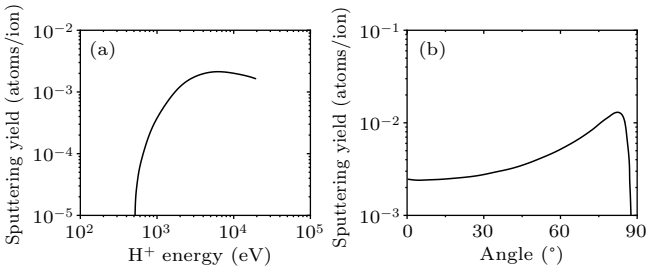


Fig. 4. (a) The sputtering yield energy dependence of H^+ ions impacting tungsten target at normal incident angle. (b) The sputtering yield angular dependence at 2000 eV.

In the angular correction factor, α is defined as the angle between the incident ion direction and the surface normal, expressed in radians. α_0 is given by the following formula:

$$\alpha_0 = \pi - \arccos\sqrt{\frac{1}{1+\dfrac{E_0}{E_{\rm sp}}}}, \tag{9}$$

where the binding energy $E_{\rm sp}$ of the incident ion species must be provided. For hydrogen isotope ions, $E_{\rm sp}$ is taken as 1 eV.[50] The sputtering yield angular dependence of incident H^+ ions and tungsten target materials combination used in our model at 2000 eV is presented in Fig. 4(b). Therefore, the number of impurity atoms sputtered out under specific ion incidence energy and angle can be calculated.

2.2.2. Emission of sputtered atoms

The key parameters of sputtered atoms upon leaving the target include their ejection position, angle, and energy. In this work, it is assumed that the ejection position of the sputtered atoms is simply where the H^+ ions bombard the target surface. And the ejection angle θ and energy E of the sputtered atoms are independent of each other.

The ejection energy of the sputtered atoms follows the Thompson distribution[51]

$$F(E)\,{\rm d}E \propto \frac{\left\{1-\sqrt{\dfrac{(U_{\rm s}+E)}{\gamma E_0}}\right\}}{E^2\left(1+\dfrac{U_{\rm s}}{E}\right)^3}{\rm d}E, \tag{10}$$

where E_0 is the energy of the incident ions, $U_{\rm s}$ is the surface binding energy of the target, and γ is the reduced mass. The probability density function for the energy of sputtered atoms at a specified incident ion energy can then be derived based on Eq. (10). The rejection sampling method is used to sample the energy of the sputtered atoms, ensuring that the total energy of all sputtered atoms cleared by the ion statistically follows the Thompson distribution.[51]

Finally, the ejection angle θ of the sputtered atoms is determined, which is the angle between the surface normal and the particle ejection direction. The number of atoms sputtered into the solid angle ${\rm d}\Omega$ is proportional to $\cos^n\theta\,{\rm d}\Omega$.[52,53] Typically, n is between 1 and 2. The ejection angle used in the Monte Carlo calculations is generated by using the inverse transformation method[54]

$$\theta = \cos^{-1}\left(\gamma^{\frac{1}{n}}\right), \tag{11}$$

where γ is a uniformly distributed random number between 0 and 1.

Therefore, when an ion impacts the limiter surface and causes impurity sputtering, the number, energy, and angle of the sputtered impurity atoms can all be determined. By tracking the motion of the sputtered atoms, we can then obtain their density distribution in space after a certain period.

3. Simulation results and discussion

Figures 5(a)–5(c) display the time-averaged distributions of electric potential and figures 5(d)–5(f) display the H^+ ion density profiles for $V_{\rm RF} = 200$ V, 600 V, 1000 V, respectively. The other discharge conditions remain consistent and are introduced in Section 2. Under the influence of the electric and magnetic fields, the volumetric plasma gradually diffuses from the boundary toward the entire simulation area, forming a certain thickness of sheath at the edge of the grounded components, as depicted in Figs. 5(a)–5(c). A large potential drop develops inside the sheath, which induces an electric field directed from the plasma region toward the limiter surface, accelerating the hydrogen ions to bombard the limiter surface. With increasing $V_{\rm RF}$, the sheath thickness expands, as shown in Figs. 5(d)–5(f), along with a larger potential drop.

Correspondingly, the energy density distributions of the incident ions (IEDF) on the limiter surface (from $y = 0$ cm down to $y = 1$ cm) over ten radio frequency periods after the discharge stabilization are illustrated in Figs. 6(a)–6(c) for $V_{\rm RF} = 200$ V, 600 V, 1000 V, respectively. At a very low $V_{\rm RF} = 200$ V, the ion energy is primarily concentrated around 200 eV, with the maximum ion energy not exceeding 600 eV. As $V_{\rm RF}$ increases, the overall ion energy is enhanced, as shown in Figs. 6(b) and 6(c), where the energies are concentrated at approximately 500 eV and 900 eV, respectively. It can also be seen that the incident ion flux decreases from the upper edge ($y = 1$ cm) to the lower edge ($y = 0$ cm) of the limiter, which corresponds to the density distribution in the SOL plasma. This suggests that the area near the upper edge of the RF-antenna limiter may be the primary source of tungsten impurities. Therefore, it is advisable to suppress impurity sput-

tering — either by applying a coating or utilizing low-Z materials — within 0.2 cm of the upper edge of the RF-antenna limiter. Such measures could significantly mitigate the impact of tungsten impurities. In the lower region of the limiter ($Y < 0.2$ cm), a significant decline in the number of incident ions is observed, as illustrated in Fig. 6. This decrease is attributed to the formation of an RF sheath on the surface of the Faraday screen at the lower boundary of the simulation area, as depicted in Fig. 5, which further reduces the plasma density in this region. Consequently, the generation of tungsten impurities at the lower edge of the RF-antenna limiter is relatively minimal.

Based on the above incident ion angle and energy information on the limiter surface, the ejection flux of impurities sputtered from different position on the limiter surface was calculated by using the sputtering model, which is displayed in Fig. 7. The sputtered atom ejection flux increases gradually from the lower edge to the upper edge of the limiter, which corresponds to the incident ion flux distribution shown in Fig. 6.

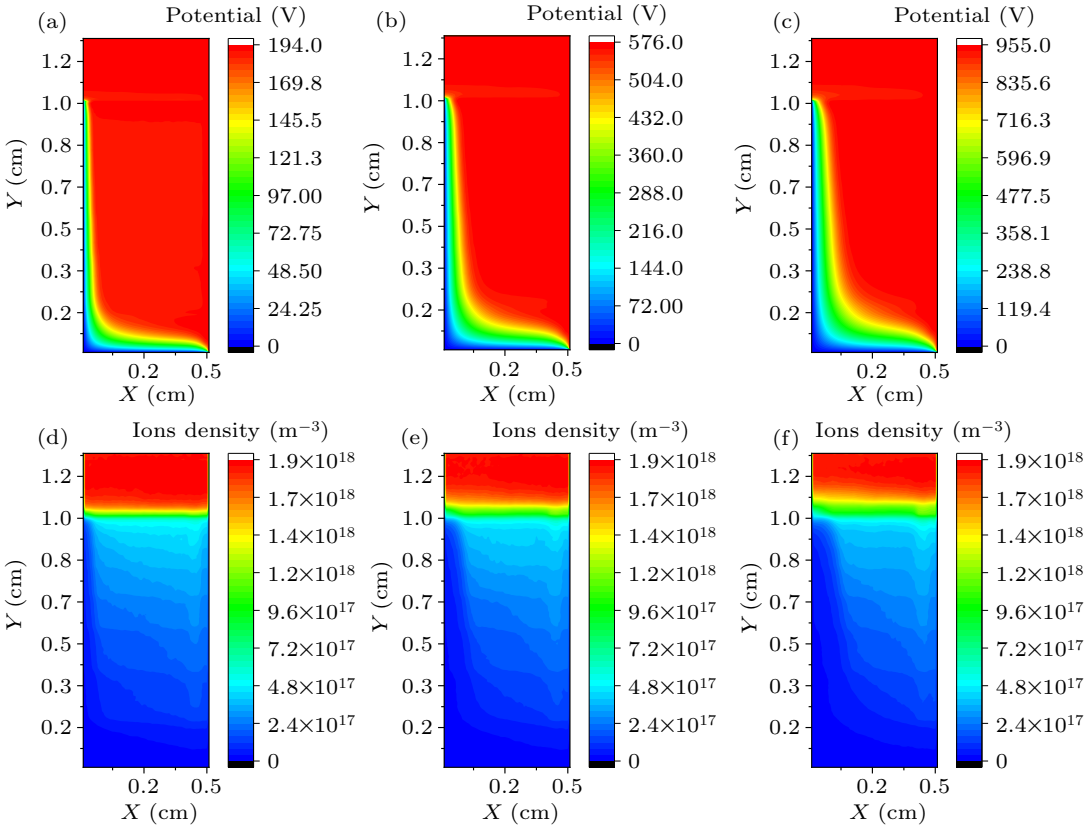


Fig. 5. (a)–(c) The time-averaged distributions of electric potential and (d)–(f) the time-averaged H^+ ion density profiles for $V_{RF} = 200$ V, 600 V, 1000 V, respectively.

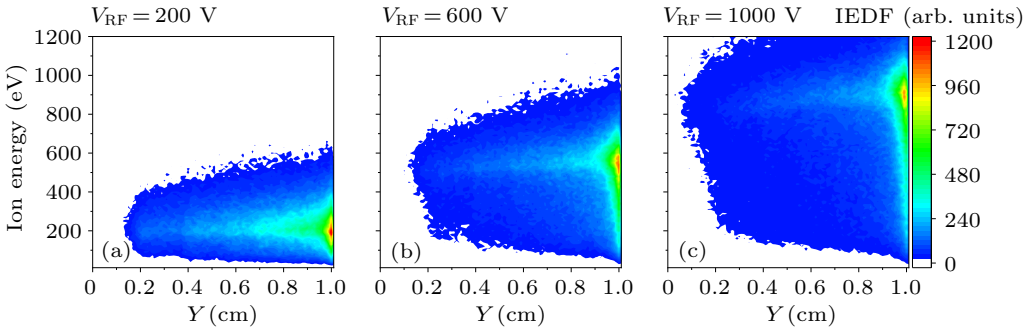


Fig. 6. (a)–(c) The ions energy density distributions (IEDF) at different position of the limiter surface for $V_{RF} = 200$ V, 600 V, 1000 V, respectively.

It can also be observed that at $V_{RF} = 200$ V, the sputtered tungsten atom flux is significantly weak (the black line), indicating that the impurity sputtering is extremely low. This is because the incident ion energy is generally distributed below 400 eV, which has not yet reached the sputtering threshold of the tungsten target material. The energy transferred from the H^+ ions to the tungsten atoms in the target is insufficient to allow the tungsten atoms to overcome the surface binding energy and be ejected, thus preventing sputtering removal. However, at $V_{RF} = 600$ V, a significant sputtering process occurs on the

surface (the red line). At this point, a large number of ions have energies exceeding the sputtering threshold, as shown in Fig. 4(a), thereby leading to the sputtering removal. The number of sputtered particles rapidly increases as the ions transfer more energy to the wall material. That is why when increasing V_{RF} to 1000 V, the sputtered atom flux increases significantly (the blue line), corresponding to the rapid increase in sputtering yield shown in Fig. 4(a). We can conclude that, for target materials such as tungsten, which possess a high sputtering threshold, reducing the incident ion energy potentially even below the sputtering threshold proves to be an effective strategy for minimizing impurity sputtering.

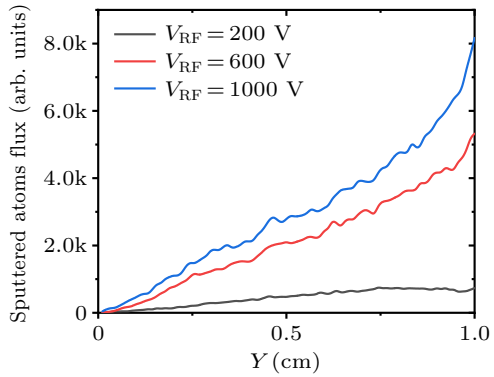


Fig. 7. The ejection flux of impurities sputtered from different positions on the limiter surface for V_{RF} = 200 V, 600 V, 1000 V, respectively.

The sputtering model additionally tracks the trajectory of each ejected atom by sampling the three-dimensional velocity of each sputtered atom, which facilitates its motion analysis near the limiter surface, generating the spatial distributions of sputtered tungsten atoms depicted in Figs. 8(a)–8(c) for V_{RF} = 200 V, 600 V, 1000 V. The spatial distributions of sputtered tungsten atoms are simulated in a larger area (2 cm along the y-axis and 3 cm along the x-axis) than the plasma simulation geometry (1.25 cm along the y-axis and 0.5 cm along the x-axis). This expanded simulation domain enables a more comprehensive analysis of the impact of the sputtered tungsten atoms. As illustrated in Fig. 7, the density of sputtered atoms is significantly lower at V_{RF} = 200 V due to the high sputtering threshold of the tungsten target material. It is therefore suggested that reducing the RF voltage across the limiters may be an effective strategy for suppressing the sputtering process. This reduction can be achieved by optimizing antenna configurations, including parameters such as antenna geometry, phase angle, and coupling impedance. At larger V_{RF}, sputtered particles may either migrate toward the Faraday screen material, potentially resulting in additional sputtering, or they may travel toward the reactor center, thereby affecting heating efficiency. Given that ions induce sputtering across the majority of the limiter and that the limiter is situated very close to the Faraday screen, the subsequent sputtering and the reflection of impurities are non-negligible factors, which will be explored in our future work. Furthermore, sputtered tungsten atoms typically move toward the reactor center within 45° relative to the magnetic field lines, as ions predominantly bombard the limiter along the direction of the magnetic field lines. This orientation makes it difficult for tungsten atoms to be ejected from the limiter at angles close to 90°.

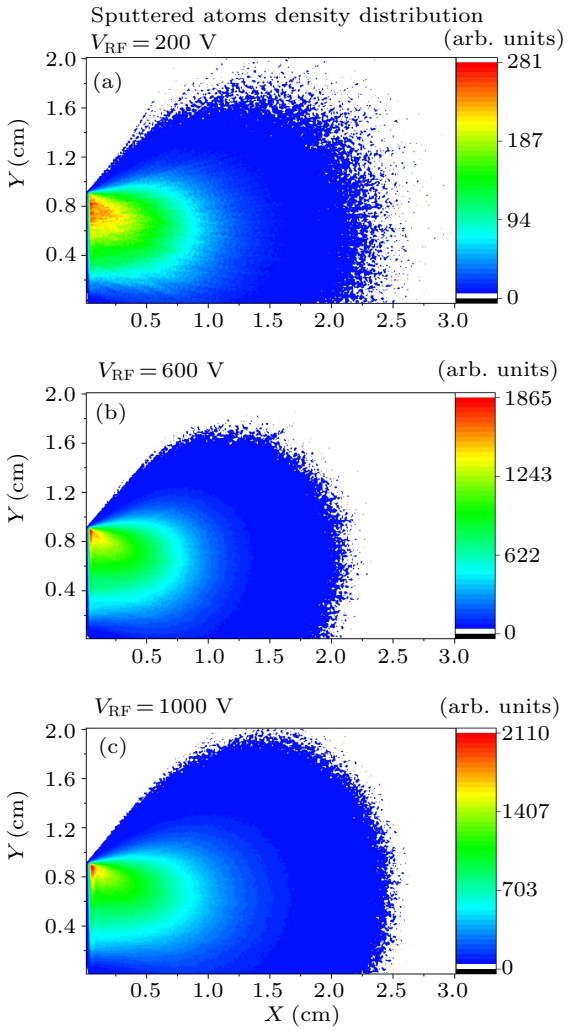


Fig. 8. (a)–(c) The spatial distributions of sputtered tungsten atoms for V_{RF} = 200 V, 600 V, 1000 V, respectively.

By integrating the spatial distribution of impurity atoms with other models, researchers can further investigate the effects of impurity sputtering on plasma stability and relevant physical phenomena.

4. Conclusion

We present a robust simulation method for calculating impurity sputtering near the ICRF antenna, which has significant implications for improving the performance of ICRH systems. This method effectively integrates an RF sheath model with a physical sputtering one, enabling to calculate sputtering yields and predict impurity distributions under various conditions. The RF sheath simulation employs a PIC model to accurately

assess ion dynamics within the sheath, yielding precise multi-dimensional ion data that impact the limiter. The sputtering model fully incorporates energy and angular dependencies, thereby enhancing its accuracy and broad applicability. We further examined the effectiveness of this model through simulations of hydrogen ion sputtering on a tungsten limiter. By comparing sputtering yields across different parameters, we conclude that controlling the RF sheath to reduce the energy of ions incident on the limiter below the sputtering threshold can effectively decrease sputtering yields. Future applications of this method may be pivotal in guiding the design and operational strategies of fusion reactors, particularly in minimizing impurity sputtering, thereby ensuring prolonged integrity of PFCs and enhancing plasma stability.

Program availability

The source code is openly available in Science Data Bank at https://doi.org/10.57760/sciencedb.j00113.00176.

Acknowledgements

This work was financially supported by the National MCF Energy R&D Program (Grant No. 2022YFE03190100), the National Natural Science Foundation of China (Grant Nos. 12422513, 12105035, and U21A20438), and the Xiaomi Young Talents Program.

References

[1] Toschi R 1997 *Fusion Engineering and Design* **36** 1
[2] Colas L, Vulliez K, Basiuk V and Tore Supra Team 2009 *Fusion Science and Technology* **56** 1173
[3] Ongena J, Messiaen A, Kazakov Y O, Koch R, Ragona R, Bobkov V, Crombé K, Durodié F, Goniche M, Krivska A, Lerche E, Louche F, Lyssoivan A, Vervier M, Eester D V, Schoor M V, Wauters T, Wright J and Wukitch S 2017 *Plasma Phys. Control. Fusion* **59** 054002
[4] Jacquinot J 1988 *Plasma Phys. Control. Fusion* **30** 1467
[5] Freidberg J P 2008 *Plasma physics and fusion energy* (Cambridge: Cambridge University Press)
[6] Jacquinot J, Bhatnagar V P, Cordey J G, *et al*. 1999 *Nucl. Fusion* **39** 235
[7] Greenwald M 2020 *Journal of Plasma Physics* **86** 861860501
[8] D'Ippolito D A and Myra J R 2011 *Journal of Nuclear Materials* **415** S1001
[9] Myra J R, D'Ippolito D A and Gerver M J 1990 *Nucl. Fusion* **30** 845
[10] Colas L, Costanzo L, Desgranges C, Brémond S, Bucalossi J, Agarici G, Basiuk V, Beaumont B, Bécoulet A and Nguyen F 2002 *Nucl. Fusion* **43** 1
[11] Wukitch S J, Lipschultz B, Marmar E, Lin Y, Parisot A, Reinke M, Rice J and Terry J 2007 *Journal of Nuclear Materials* **363–365** 491
[12] Klepper C C, Borodin D, Groth M, Lasa A, Airila M, Bobkov V, Colas L, Jacquet P, Kirschner A, Terra A, Biewer T M, Delabie E, Giroud C and JET Contributors 2016 *Phys. Scr.* **T167** 014035
[13] Causey R A and Venhaus T J 2001 *Phys. Scr.* **2001** 9
[14] Van Vugt D C, Huijsmans G T A, Hoelzl M, Loarte A, ASDEX Upgrade Team and Eurofusion MST1 Team 2019 *Phys. Plasmas* **26** 042508
[15] Urbanczyk G, Zhang X J, Zhang L, *et al*. 2020 *Nucl. Fusion* **60** 126003
[16] Urbanczyk G, Colas L, Zhang X J, *et al*. 2020 23*RD Topical Conference on Radioferquency Power in Plasmas* (Hefei, China) p. 030012
[17] Elias M, Curreli D, Jenkins T G, Myra J R and Wright J 2019 *Phys. Plasmas* **26** 092508
[18] Elias M, Curreli D and Myra J R 2021 *Phys. Plasmas* **28** 052106
[19] Bobkov V, Balden M, Bilato R, Braun F, Dux R, Herrmann A, Faugel H, Fünfgelder H, Giannone L, Kallenbach A, Maier H, Müller H W, Neu R, Noterdaeme J M, Pütterich T, Rohde V, Tsujii N, Zeus F, Zohm H and the ASDEX Upgrade Team 2013 *Nucl. Fusion* **53** 093018
[20] Li Y, Fedorczak N, Xu G S, Liang Y, Brezinsek S, Morales J and The WEST Team 2023 *Nucl. Fusion* **63** 026019
[21] Meyer O, Giacalone J C, Gouin A, Pascal J Y, Klepper C C, Fedorczak N, Lotte P, Unterberg E A, Fehling D T and Harris J H 2018 *Rev. Sci. Instrum.* **89** 10D105
[22] Zhang L, Morita S, Xu Z, Wu Z, Zhang P, Wu C, Gao W, Ohishi T, Goto M and Shen J 2015 *Rev. Sci. Instrum.* **86** 123509
[23] Myra J R, Elias M T, Curreli D and Jenkins T G 2020 *Nucl. Fusion* **61** 016030
[24] Donkó Z, Derzsi A, Vass M, Horváth B, Wilczek S, Hartmann B and Hartmann P 2021 *Plasma Sources Sci. Technol.* **30** 095017
[25] Vahedi V and Surendra M 1995 *Computer Physics Communications* **87** 179
[26] Petrov G M and Davis J 2011 *Phys. Plasmas* **18** 073102
[27] Petrov G M and Davis J 2008 *Computer Physics Communications* **179** 868
[28] Mason R J 1987 *Journal of Computational Physics* **71** 429
[29] Verboncoeur J P 2005 *Plasma Phys. Control. Fusion* **47** A231
[30] Birdsall C K and Langdon A B 2018 *Plasma physics via computer simulation* (Boca Raton: CRC press)
[31] Li Y, Wang W, Su X, Zhang G and Tang H 2024 *Phys. Scr.* **99** 055604
[32] Yang S and Gobbert M K 2009 *Appl. Math. Lett.* **22** 325
[33] Jacquot J, Milanesio D, Colas L, Corre Y, Goniche M, Gunn J, Heuraux S and Kubič M 2014 *Phys. Plasmas* **21** 061509
[34] Qin C, Zhang X, Zhao Y, Wan B, Braun F, Wang L, Yang Q, Yuan S and Cheng Y 2015 *Plasma Science and Technology* **17** 167
[35] Myra J R, D'Ippolito D A and Ho Y L 1996 *Fusion Engineering and Design* **31** 291
[36] Yang H, Wu C F, Dong S, Zhao Y P, Zhang X J and Shang L 2016 *Nucl. Sci. Tech.* **27** 46
[37] Bultinck E, Kolev I, Bogaerts A and Depla D 2008 *J. Appl. Phys.* **103** 013309
[38] Vahedi V and DiPeso G 1997 *Journal of Computational Physics* **131** 149
[39] Messiaen A, Koch R, Weynants R R, Dumortier P, Louche F, Maggiora R and Milanesio D 2010 *Nucl. Fusion* **50** 025026
[40] Stangeby P C 2000 *The plasma boundary of magnetic fusion devices* (Boca Raton: CRC press)
[41] Wang H, Jiang W and Wang Y 2010 *Plasma Sources Sci. Technol.* **19** 045023
[42] Gauthier E, Eckstein W, László J and Roth J 1990 *Journal of Nuclear Materials* **176–177** 438
[43] Eckstein W 1997 *Journal of Nuclear Materials* **248** 1
[44] Sigmund P 1987 *Nuclear Instruments and Methods in Physics Research Section B: Beam Interactions with Materials and Atoms* **27** 1
[45] Eckstein W, Garcia-Rosales C, Roth J and László J 1993 *Nuclear Instruments and Methods in Physics Research Section B: Beam Interactions with Materials and Atoms* **83** 95
[46] Yuan J, Li X, Guan L, Liu Z, Dong S, Yang Y, Xu K and Zhuang S 2023 *Optical Materials Express* **13** 1249
[47] Liu Z X, Li X Y, Zhang Q Z, Schulze J, Zhang R B and Wang Y N 2024 *Journal of Vacuum Science & Technology A* **42** 053006
[48] Eckstein W, Stephens J A, Clark R E H, Davis J W, Haasz A A, Vietzke E and Hirooka Y 2001 *Atomic and plasma-material interaction data for fusion V 7, part B Particle induced erosion of Be, C and W in fusion plasmas Part B: Physical sputtering and radiation-enhanced sublimation. International Atomic Energy Agency (IAEA): IAEA*
[49] Behrisch R, Sigmund P, Robinson M T, Andersen H H, Bay H L and Roosendaal H E 1981 *Sputtering by particle bombardment 1. Physical sputtering of single-element solids* (Heidelberg, Springer Berlin)
[50] Eckstein W 1991 *Computer Simulation of Ion-Solid Interactions* (Heidelberg, Springer Berlin)
[51] Turner G M, Falconer I S, James B W and McKenzie D R 1989 *J. Appl. Phys.* **65** 3671
[52] Turner G M, Falconer I S, James B W and McKenzie D R 1992 *J. Vacuum Sci. Technol. A: Vacuum Surf. Films* **10** 455
[53] Sobbia R, Browning P K and Bradley J W 2008 *J. Vacuum Sci. Technol. A: Vacuum Surf. Films* **26** 103
[54] Samuel S M Wong 1997 *Computational Methods in Physics and Engineering 2nd Edition* (Singapore: World Scientific Press)